




Different temperature sensitivities of key physiological processes lead to divergent trait response patterns in Arctic phytoplankton

Linda Rehder ^{1,*} Sebastian D. Rokitta ¹ Clara J. M. Hoppe ¹ Isabelle Buschmann ^{1,2}
Levke Jasper ^{1,3} Björn Rost ^{1,4}

¹Marine Biogeosciences, Alfred Wegener Institute, Helmholtz Centre for Polar and Marine Research, Bremerhaven, Germany

²Department Biology I (Botany), Ludwig Maximilian University, Munich, Germany

³Plankton Ecology Lab, Institute for Chemistry and Biology of Marine Environments, Carl von Ossietzky University of Oldenburg, Wilhelmshaven, Germany

⁴Faculty of Biology and Chemistry, University of Bremen, Bremen, Germany

Abstract

Ocean warming is especially pronounced in the Arctic, and phytoplankton will face thermodynamically driven changes in their physiology, potentially pushing them beyond their thermal optimum. We assessed temperature responses of multiple functional traits over their entire thermal window (growth rates, quotas of particulate organic carbon, nitrogen, and chlorophyll *a*, as well as photophysiological parameters) in three different Arctic phytoplankton species (*Thalassiosira hyalina*, *Micromonas pusilla*, and *Nitzschia frigida*). Temperature response patterns in growth and biomass production rates indicated that all species exhibit wide thermal windows with highest rates at temperatures that exceed current polar temperatures. Species showed different temperature response patterns in cellular elemental quotas, which originate from the interplay of cell division and biomass production: These processes differ in their temperature sensitivity and optima, resulting in U-shaped, bell-shaped, or linear patterns of elemental quotas. Despite unaltered light intensity, higher temperatures increased light acclimation indices in all species while lifetimes of photosystem II reopening decreased in all species, suggesting that warming causes a transition from light saturation to light limitation. Our findings on temperature sensitivities of cell division and biomass production not only indicate that Arctic phytoplankton may benefit from moderate warming, but also highlight that meaningful interpretations of cellular quotas require a consideration of the underlying processes.

The Arctic is one of the regions most affected by climate change, with warming rates more than three times the global average (Rantanen et al. 2022). Alongside with rising mean temperatures, heatwaves have become more frequent, intense, and longer lasting in this region (Hobday et al. 2016; Cooley et al. 2022). Model simulations project further warming, especially in the ever-extending ice-free regions (Constable et al. 2022). In contrast to many other

climate-related changes, like sea-ice decline or ocean acidification, warming itself has probably the most direct and potentially largest impact on polar species and ecosystems. Responses at the base of the ecosystems are hereby most relevant since changes in primary productivity are likely to propagate and amplify through the food web (Stock et al. 2014).

Phytoplankton and ice algae face many challenges in the Arctic Ocean. Being phototrophs, their growth is strongly controlled by light availability, but also the low temperatures prevailing in polar waters. Despite the absence of primary production during polar night, Arctic phytoplankton contributes significantly to global primary production (Van Leeuwe et al. 2018). Arctic sea-ice loss leads to deeper light penetration, longer growing seasons as well as an enlarged habitat for open ocean algae, which has been argued to drive substantial increases in net primary production (Ardyna and Arrigo 2020; Lewis et al. 2020). The earlier onset and accelerated biomass buildup due to altered light and temperature conditions may result in earlier phytoplankton spring blooms

*Correspondence: linda.rehder@awi.de

Additional Supporting Information may be found in the online version of this article.

This is an open access article under the terms of the [Creative Commons Attribution-NonCommercial](https://creativecommons.org/licenses/by-nc/4.0/) License, which permits use, distribution and reproduction in any medium, provided the original work is properly cited and is not used for commercial purposes.

Author Contribution Statement: Design of the research: LR, SR, CJMH, and BR. Conduct the research: LR, IB, and LJ. Data analysis: LR, SR, CJMH, IB, LJ, and BR. Drafting, revision, and editing of the manuscript: LR with contribution of all coauthors.

with higher peak biomass (Tedesco et al. 2019; Ardyna and Arrigo 2020; Rokitta et al. 2023), but also more prominent nutrient limitation over summer months (Wassmann and Reigstad 2011; Tremblay et al. 2015). While the aforementioned consequences of changes in the light regime are reasonably well understood and often used for projections, there are uncertainties with regard to the direct effects of warming on primary producers, specifically regarding optimal temperatures of different physiological processes.

As a universal driver, temperature affects all physical and (bio)chemical processes. Ectothermic organisms like phytoplankton are thus affected by temperature-induced changes of enzyme activity, membrane fluidity, or electron transfer rates, which are in turn reflected in processes underlying photosynthesis, respiration, nutrient assimilation, and cell division (Raven and Geider 1988; Falkowski et al. 1998). Typically, cell division (i.e., growth rate) as well as primary production follow an optimum curve (Thomas et al. 2012; Baker et al. 2016; Barton and Yvon-Durocher 2019), so that processes are stimulated by warming up to a certain optimum beyond which they sharply decline, for example, due to thermal inactivation of enzymes or increasing accumulation of reactive oxygen species (Moreno et al. 2024). Moreover, the temperature sensitivity of single physiological subprocesses likely differs, requiring readjustments of thermodynamically induced imbalances between those processes over the course of acclimation (Rehder et al. 2023). Since respiratory processes are often claimed to be more intensely stimulated than photosynthetic processes (Padfield et al. 2016; Barton et al. 2020), it is expected that ecosystems become more heterotrophic with warming (Hoppe et al. 2002; Hancke and Glud 2004; Holding et al. 2013). Furthermore, temperature was found to alter phytoplankton community composition (Hare et al. 2007; Kling et al. 2020; Ahme et al. 2023, 2024). In the Arctic, data from remote sensing, genetic field surveys, and sediment traps indeed suggest that species compositions shift from diatom-dominated toward *Phaeocystis*-dominated communities with warming (Nöthig et al. 2015; Soltwedel et al. 2016; Orkney et al. 2020), which will likely have substantial effects on food web dynamics and carbon export (Wiedmann et al. 2020; Assmy et al. 2023).

To understand the effect of ocean warming on phytoplankton, it is necessary to investigate how ecologically relevant phytoplankton species respond to temperature in different functional traits such as cell division, biomass production, or elemental stoichiometry. While previous studies focused mostly on growth rates over time scales of adaptation and evolution (Listmann et al. 2016; Schaum et al. 2017; Barton et al. 2023), we here focus on several traits and their physiological underpinnings on acclimation

time scales. To this end, we incubated *Thalassiosira hyalina*, a centric diatom that often dominates Arctic pelagic spring blooms (Hegseth and Sundfjord 2008), the picoeukaryote *Micromonas pusilla*, which substantially contributes to the largely mixotrophic winter community (Vader et al. 2015), and *Nitzschia frigida*, a typical ice-associated pennate diatom (Syvertsen 1991). We hypothesized that the investigated species occupy different thermal niches, according to their differences in habitat and seasonal distribution, and that functional traits exhibit different temperature sensitivities, which should become most prominent at the “edges” of their thermal windows.

Methods

Culturing

Strains of *T. hyalina* (KB3 SS5; Kongsfjord 2020), *M. pusilla* (CLP 1; Kongsfjord 2014) and *N. frigida* (UIO-542, Fram Strait 2019) were cultivated in triplicates in 0.2 μm sterile-filtered Arctic seawater (Salinity 32), which was enriched with vitamins and trace metals according to F/2 medium (Guillard and Ryther 1962). Nitrate, silicate, and phosphate were added in concentrations of 100, 100, and 6 $\mu\text{mol L}^{-1}$, respectively. Cells were grown as semi-continuous dilute batch cultures using custom-made 1-liter cylindrical glass bottles. Cultures were aerated with air containing a pCO_2 of 400 μatm generated by a gas mixing system (CMG 2000, MCZ Umwelttechnik), in which CO_2 -free air (< 1 ppm CO_2 ; Domnick Hunter) was mixed with pure CO_2 (Air Liquide). Acclimation temperatures ranged between 0°C and 14°C, depending on the species-specific thermal window that is defined as the temperature range in which cultures exhibit growth rates $\geq 0 \text{ d}^{-1}$. To ensure light saturation without photodamage, cell cultures were illuminated at 100 $\mu\text{mol photons m}^{-2} \text{ s}^{-1}$ (*T. hyalina* and *M. pusilla*) or 30 $\mu\text{mol photons m}^{-2} \text{ s}^{-1}$ (*N. frigida*, due to its association with sea-ice) in a 16:8 h light : dark cycle ensuring synchronized cell division. In the acclimations, cell concentrations remained low to ensure nutrient replete conditions and quasi-stable carbonate chemistry (pH drift < 0.05).

Cell division rate assessments and fitting of temperature responses

Before the start of the experiment, species were grown under the experimental treatment conditions at least for 10 generations, and full acclimation was confirmed by stable growth rates over at least 3 consecutive days. After acclimation was ensured, rate estimates were based on daily samplings, which took place about 4 h after the start of the photoperiod. Cell concentrations were determined using a cell counter (Beckmann-Coulter Multisizer III), and specific growth rates (i.e., using the base e) were calculated using the daily

increments of cell concentrations during the exponential growth phase according to the formula:

$$\mu = \frac{\ln(N_1) - \ln(N_0)}{t_1 - t_0} \quad (1)$$

where μ is the specific growth rate (d^{-1}), and N_0 as well as N_1 are the cell concentrations at the initial and final time points t_0 and t_1 , respectively.

Temperature response curves of growth rates were fitted by least squares regression, applying the solver function of Microsoft Excel 2016 across all biological replicates per species at once. We hereby used the Eppley function (Eppley 1972) modified by Norberg et al. (2004) as the following:

$$\mu(T) = \left(1 - \left(\frac{T-z}{w}\right)^2\right) a e^{bT} \quad (2)$$

where w refers to the theoretical thermal niche width (later referred to as thermal window), z refers to the temperature where μ is equal to the Eppley function, and a and b are parameters of the Eppley function. This function was also used to derive the lower (T_{\min}) and upper temperatures (T_{\max}), beyond which the growth rate equals zero. Since the fit procedure yielded T_{\min} values lower than the freezing point of seawater, we set this value to -1.8°C , in accordance with the freezing temperature of our sea water. The thermal window (T_{window}) was then calculated as the difference of T_{\max} and T_{\min} . The calculated optimal temperature (T_{opt}) was obtained via the derivative of Eq. 2 following:

$$T_{\text{opt}} = \frac{bz - 1 + \sqrt{\left(\frac{w}{2}\right)^2 b^2 + 1}}{b} \quad (3)$$

The calculated maximal growth rate (μ_{\max}) was obtained from inserting T_{opt} into Eq. 2. Subsequently, we determined the temperature range where μ was $\geq 80\%$ of μ_{\max} and highlighted this temperature range in each plot (Figs. 1–6) with a light green band.

Elemental composition and pigmentation

Sampling for cellular quotas of particulate organic carbon (POC) and nitrogen (PON) as well as of chlorophyll *a* (Chl *a*) was performed during exponential growth after acclimation for at least 10 d or seven generations. For the determination of POC and PON, cells were filtered onto precombusted (12 h, 500°C) glass fiber filters (GF/F, $0.7 \mu\text{m}$ nominal pore size, Whatman). After drying for at least 24 h, filters were submitted to elemental analysis (EuroVector EA 3000) using the flash combustion technique (Knap et al. 1996). Due to compromised PON analyses for *T. hyalina* and *M. pusilla*, only PON quotas of *N. frigida* could be obtained. POC production rates were calculated from POC quotas and specific growth rates per biological replicate following Morel (1987):

$$\text{POC production} = \mu \times \text{POC quota} \quad (4)$$

Chl *a* samples were filtered onto pre-combusted (12 h, 500°C) glass fiber filters (GF/F $0.7 \mu\text{m}$, Whatman), shock-frozen in liquid nitrogen and stored at -80°C until extraction. Filters were extracted overnight in 5 mL acetone (90%, Sigma-Aldrich), after cell disruption in a cell-mill (Precellys 24, Bertin). Then, extracts were centrifuged (4500 rpm for 7 min, Sigma 4K10) and Chl *a* concentration in the supernatant was determined using the fluorometric “acidification-method” (Turner Trilogy, Turner Designs; Knap et al. 1996). Samples of *N. frigida* were measured using a TD-700 Fluorometer (Turner Designs) after intercalibration of instruments. Ratios of Chl *a* : POC were subsequently calculated per biological replicate.

Chl *a*-based variable fluorescence

Photophysiological characteristics based on photosystem (PS) II variable fluorescence measurements were assessed using a fast repetition rate fluorometer (FRRf; FastOcean, Chelsea Technologies) combined with the FastAct2 Laboratory system (Chelsea Technologies). Light-emitting diodes were set to 450 nm emission wavelength to fully saturate all photosystems on short timescales. We used the FRRf in a single turnover mode, in which the saturation phase comprised 100 (*T. hyalina*), 120 (*M. pusilla*), and 110 (*N. frigida*) flashlets, respectively, on a $2\text{-}\mu\text{s}$ pitch, and the relaxation phase comprised 40 flashlets on a $60\text{-}\mu\text{s}$ pitch. All measurements were conducted in a temperature-controlled cuvette at the respective acclimation temperature after dark acclimation for at least 15 min. Minimum Chl *a* fluorescence (F_0 and F'_0 for dark- and light-acclimated measurements, respectively) and maximum Chl *a* fluorescence (F_m and F'_m for dark- and light-acclimated measurements, respectively) were obtained from iteratively fitting the induction (Kolber et al. 1998) and the relaxation phase (Oxborough 2012). Photosynthesis–irradiance (PI) curves comprised eight light levels (5 min pre-acclimation at respective actinic light per light level; maximal light levels of $\sim 900 \mu\text{mol photons m}^{-2} \text{s}^{-1}$). Basic photophysiological parameters such as maximum quantum yields of PSII in the dark (F_v/F_m) and in the light, absorption cross section of PSII (σ_{PSII}), and lifetime of PSII reopening (τ) were obtained using standard calculations (Genty et al. 1989; Maxwell and Johnson 2000; McKew et al. 2013; Schuback et al. 2017). Absolute electron transport rates (ETR) were obtained per light level according to Suggett et al. (2004) and Trimborn et al. (2017) and fitted in accordance to Rokitta and Rost (2012). ETRs at in situ irradiance of 30 or $100 \mu\text{mol photons m}^{-2} \text{s}^{-1}$, light acclimation indices (E_k) and light use efficiencies (α ; Supporting Information Table S1) were calculated accordingly. Non-photochemical quenching (NPQ) was calculated after McKew et al. (2013).

Data analysis

All data are shown as the mean of 3 biological replicates \pm standard deviation (SD), if not stated otherwise. Least squares regression analyses of linear or quadratic functions were applied to verify the shapes of temperature response patterns of functional traits. Whenever temperature response patterns are described as “U-shaped,” “bell-shaped,” or “linear increased/decreased,” trends are significant ($p \leq 0.05$). Results from regression fittings are reported in the Supporting Information (Tables S2–S4).

Results

Biological parameters

T. hyalina exhibited positive growth rates up to 12°C and presented a bell-shaped curve, with the highest measured growth rate of $1.4 \pm 0.1 \text{ d}^{-1}$ at 8°C (Fig. 1a). Between 2.5°C and 9°C, rates were $\sim 1.0 \text{ d}^{-1}$, showing a wide plateau around the optimum. POC production rates followed a similar pattern with a maximum of $567 \pm 56 \text{ pg C cell}^{-1} \text{ d}^{-1}$ at 8°C (Fig. 1a). POC quotas followed a U-shaped pattern over large parts of the investigated temperature range with maxima at 2.5°C ($476 \pm 12 \text{ pg C cell}^{-1}$) and 10°C ($465 \pm 26 \text{ pg C cell}^{-1}$; Fig. 1b). Chl *a* quotas followed a similar pattern as POC quotas (Fig. 1b). This resulted in largely unchanged Chl *a* : POC up to 8°C ($\sim 0.025 \text{ pg pg}^{-1}$; Fig. 1c), beyond which values increased to $\sim 0.04 \text{ pg pg}^{-1}$ (Fig. 1c).

M. pusilla exhibited positive growth rates up to 13°C and a symmetrical bell-shaped curve with a maximum rate of $1.0 \pm 0.03 \text{ d}^{-1}$ at 6°C (Fig. 2a). Production rates followed the same pattern with a maximum of $19.0 \pm 2.0 \text{ pg C cell}^{-1} \text{ d}^{-1}$ at 6°C (Fig. 2a). POC quotas also followed a bell-shaped pattern similar to growth and production rates, with a maximum at 10°C ($20 \pm 2 \text{ pg C cell}^{-1}$; Fig. 2b). Chl *a* quotas (Fig. 2b), in turn, remained largely unchanged over the thermal window. Chl *a* : POC ratios varied between ~ 0.001 and 0.002 pg pg^{-1}

over the tested temperature range, with yet the highest values at or above 12°C (Fig. 2c).

N. frigida exhibited positive growth rates up to 11°C and a wide bell-shaped curve with a maximum of $0.52 \pm 0.8 \text{ d}^{-1}$ at 2.5°C (Fig. 3a). Since cells formed chains below 2.5°C (Supporting Information Fig. S1), we refrained from cellular normalizations for 0°C and 1.5°C data. POC production rates were highest at intermediate temperatures ($70 \pm 9 \text{ pg C cell}^{-1} \text{ d}^{-1}$ at 5.5°C; Fig. 3a) but declined beyond 8.5°C. POC quotas increased linearly with temperature from $129 \pm 6 \text{ pg C cell}^{-1}$ at 2.5°C to $366 \pm 17 \text{ pg C cell}^{-1}$ at 11°C (Fig. 3b). Chl *a* quotas (Fig. 3b) remained largely unchanged over the investigated temperature range. This resulted in a steep linear decrease of Chl *a* : POC ratio from 0.06 pg pg^{-1} at 2.5°C to 0.02 pg pg^{-1} at 11°C (Fig. 3c). POC : PON ratios, in turn, showed a steep linear increase from $\sim 5 \text{ mol mol}^{-1}$ at 2.5°C to $\sim 15 \text{ mol mol}^{-1}$ at 11°C (Fig. 3c).

To compare temperature responses between the three different species, data on growth rates were fitted using the Eppley–Norberg function (Norberg et al. 2004; Eq. 2). *T. hyalina* exhibited the highest calculated maximal growth rate (1.22 d^{-1} ; Table 1), followed by *M. pusilla* (1.04 d^{-1} ; Table 1). *N. frigida* exhibited lower calculated maximal rates (0.40 d^{-1} ; Table 1). The derived optimal temperature for growth rate (T_{opt}) was highest in *M. pusilla* (7.6°C), followed by *T. hyalina* (7.0°C). For *N. frigida*, the derived optimal temperature was lower (4.3°C). The upper boundaries (T_{max}) were similarly high for *T. hyalina* and *M. pusilla* ($\sim 14^\circ\text{C}$), whereas *N. frigida* could only maintain growth up to $\sim 11^\circ\text{C}$. Consequently, the thermal windows ranged between $\Delta 13^\circ\text{C}$ and $\Delta 16^\circ\text{C}$ (Table 1).

Photophysiology

T. hyalina exhibited generally high values for the photosystem II (PSII) quantum yield (F_v/F_m), with a bell-shaped curve in response to temperature and an optimum of ~ 0.65 at 6°C (Fig. 4a). The absolute electron transport rate at in situ

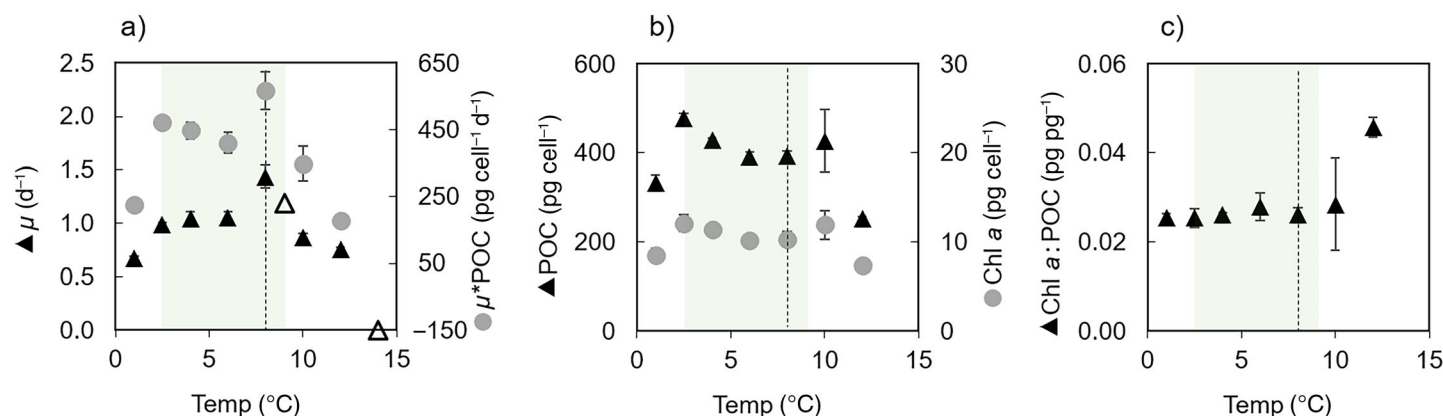


Fig. 1. Acclimation parameters of *Thalassiosira hyalina* at different temperatures. (a) Growth rates (black triangles) and POC production rates (gray circles), (b) particulate organic carbon quotas (POC; black triangles) and Chl *a* quotas (gray circles), and (c) ratios of Chl *a* : POC (black triangles). The green band defines the temperature range where μ is $\geq 80\%$ of the calculated μ_{max} and the dashed line indicates the measured optimal growth temperature. At 14°C, μ was $\leq 0 \text{ d}^{-1}$. Error bars denote standard deviation ($n = 3$), except for data where one or two replicates were lost ($n \leq 2$; empty symbols).

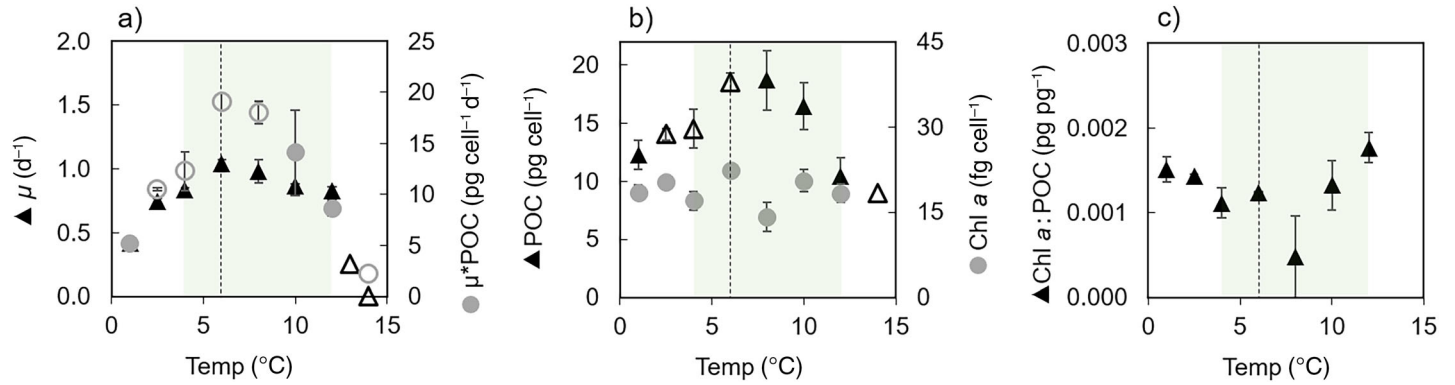


Fig. 2. Acclimation parameters of *Micromonas pusilla* at different temperatures. **(a)** Growth rates (black triangles) and POC production rates (gray circles), **(b)** particulate organic carbon quotas (POC; black triangles) and Chl *a* quotas (gray circles), and **(c)** ratios of Chl *a* : POC (black triangles). The green band defines the temperature range where μ is $\geq 80\%$ of the calculated μ_{max} , and the dashed line indicates the measured optimal growth temperature. At 14°C, μ was $\leq 0\ d^{-1}$. Error bars denote standard deviation ($n = 3$), except for data where one or two replicates were lost ($n \leq 2$; empty symbols).

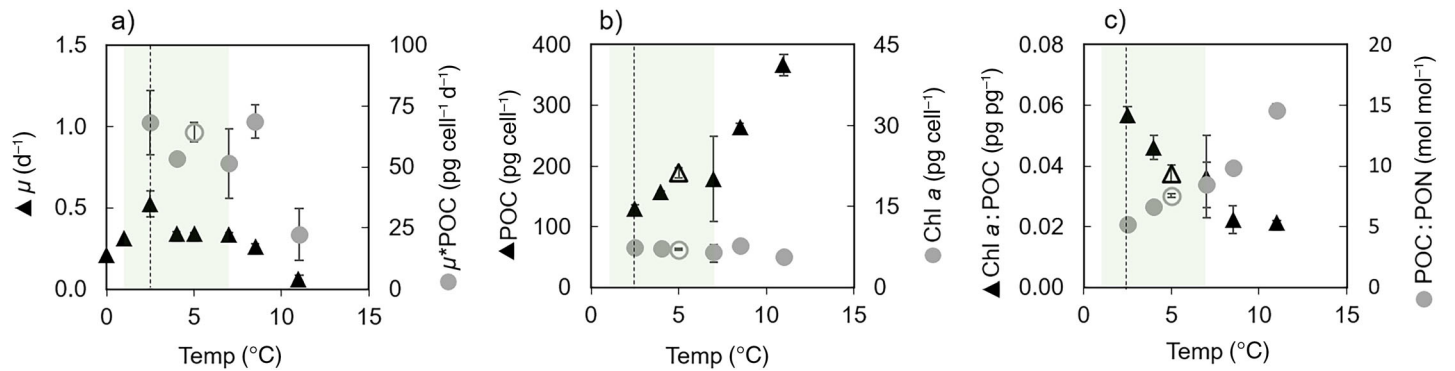


Fig. 3. Acclimation parameters of *Nitzschia frigida* at different temperatures. **(a)** Growth rates (black triangles) and POC production rates (gray circles), **(b)** particulate organic carbon quotas (POC; black triangles) and Chl *a* quotas (gray circles), and **(c)** ratios of Chl *a* : POC (black triangles) and POC : PON (gray circles). The green band defines the temperature range where μ is $\geq 80\%$ of calculated μ_{max} and the dashed line indicates the measured optimal growth temperature. Error bars denote standard deviation ($n = 3$), except for data where one or two replicates were lost ($n \leq 2$; empty symbols).

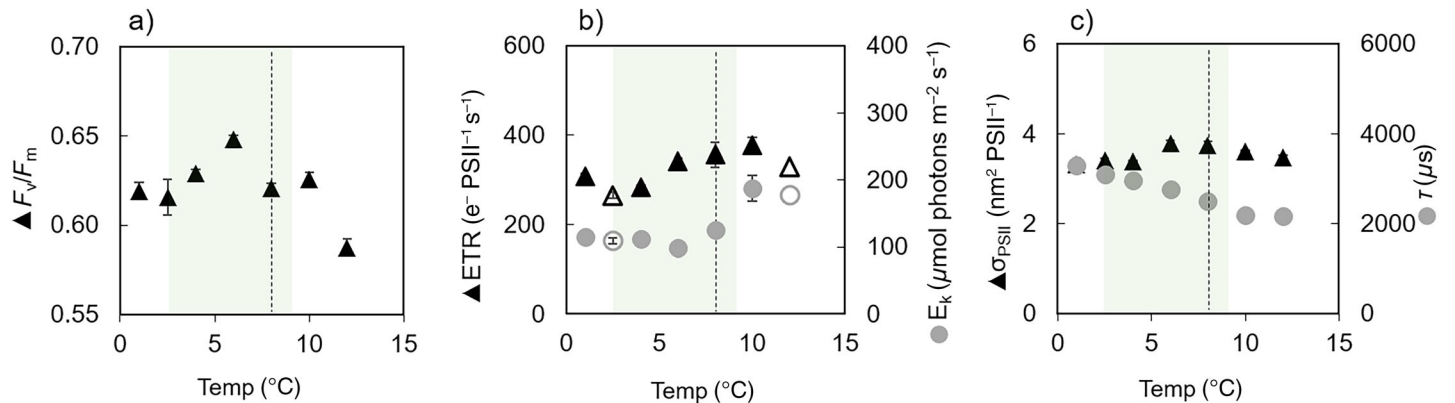


Fig. 4. Photophysiological parameters of *Thalassiosira hyalina* at different temperatures. **(a)** Photosystem II quantum yield (F_v/F_m ; black triangles), **(b)** absolute electron transport rate under in situ irradiance (ETR; black triangles) and light acclimation index (E_k ; gray circles), and **(c)** absorption cross section (σ_{PSII} ; black triangles) and life time of PSII reopening (τ , gray circles). The green band defines the temperature range where μ is $\geq 80\%$ of calculated μ_{max} and the dashed line indicates the measured optimal growth temperature. Error bars denote standard deviation ($n = 3$), except for data where one or two replicates were lost ($n \leq 2$; empty symbols).

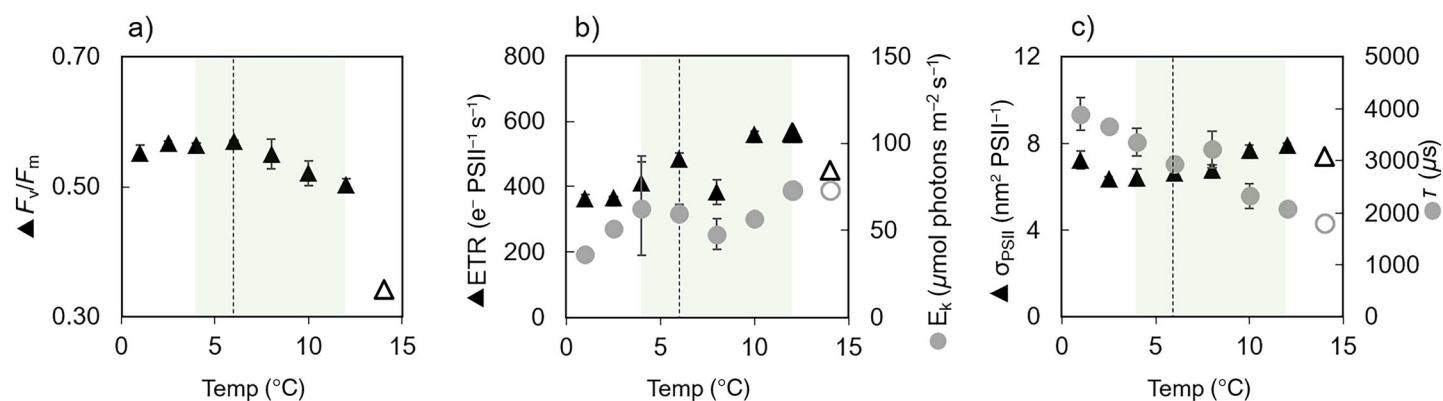


Fig. 5. Photophysiological parameters of *Micromonas pusilla* at different temperatures. **(a)** Photosystem II quantum yield (F_v/F_m ; black triangles), **(b)** absolute electron transport rate under in situ irradiance (ETR; black triangles) and light acclimation index (E_k ; gray circles), and **(c)** absorption cross section (σ_{PSII} ; black triangle) and life time of PSII reopening (τ , gray circles). The green band defines the temperature range where μ is $\geq 80\%$ of calculated μ_{max} and the dashed line indicates the measured optimal growth temperature. Error bars denote standard deviation ($n = 3$), except for data where one or two replicates were lost ($n \leq 2$; empty symbols).

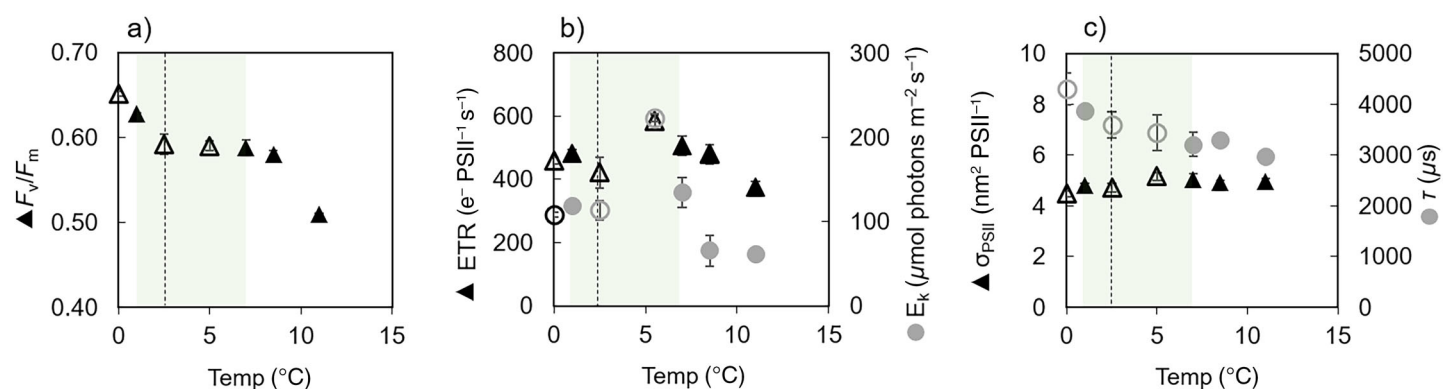


Fig. 6. Photophysiological parameters of *Nitzschia frigida* at different temperatures **(a)** photosystem II quantum yield (F_v/F_m ; black triangles), **(b)** absolute electron transport rate under in situ irradiance (ETR; black triangles) and light acclimation index (E_k ; gray circles), and **(c)** absorption cross section (σ_{PSII} ; black triangle) and life time of PSII reopening (τ , gray circles). The green band defines the temperature range where μ is $\geq 80\%$ of calculated μ_{max} and the dashed line indicates the measured optimal growth temperature. Error bars denote standard deviation ($n = 3$), except for data where one or two replicates were lost ($n \leq 2$; empty symbols).

irradiance (ETR) followed a bell-shaped curve between 2.5°C and 12°C with an optimum of $\sim 400 e^- \text{PSII}^{-1} \text{s}^{-1}$ at 10°C (Fig. 4b). The light acclimation index (E_k) remained constant until the optimal growth temperature at $\sim 110 \mu\text{mol photons m}^{-2} \text{s}^{-1}$, but increased up to $\sim 190 \mu\text{mol photons m}^{-2} \text{s}^{-1}$ beyond (Fig. 4b). The absorption cross section (σ_{PSII}) followed a shallow bell-shaped curve similar to F_v/F_m with an optimum of $\sim 3.8 \text{ nm}^2 \text{PSII}^{-1}$ at 6°C (Fig. 4c). The lifetime of PSII reopening (τ) decreased linearly from ~ 3300 to $\sim 2200 \mu\text{s}$ over the investigated temperature range (Fig. 4c).

M. pusilla exhibited a wide bell-shaped curve for F_v/F_m with an optimum of 0.57 at 6°C (Fig. 5a), followed by a steep decline to 0.34 at 14°C. The ETR also followed a bell-shaped temperature response pattern with an optimum of $\sim 600 e^- \text{PSII}^{-1} \text{s}^{-1}$ at 10°C (Fig. 5b). E_k increased from ~ 35 to

$\sim 75 \mu\text{mol photons m}^{-2} \text{s}^{-1}$ (Fig. 5b). Except for lowest and highest investigated temperatures, σ_{PSII} followed a similar pattern, that is, it increased between 2.5°C and 12°C from ~ 6.4 to $7.9 \text{ nm}^2 \text{PSII}^{-1}$, and decreased to $\sim 7.4 \text{ nm}^2 \text{PSII}^{-1}$ at 14°C (Fig. 5c). τ decreased linearly from ~ 3900 to $1800 \mu\text{s}$ over the investigated temperature window (Fig. 5c).

N. frigida exhibited a decreasing trend in F_v/F_m with a plateau of ~ 0.59 between 2.5°C and 9°C (Fig. 6a). The ETR followed a bell-shaped temperature response pattern with an optimum of $\sim 600 e^- \text{PSII}^{-1} \text{s}^{-1}$ at 5°C (Fig. 6b). E_k increased until $\sim 220 \mu\text{mol photons m}^{-2} \text{s}^{-1}$ at 5°C and declined beyond (Fig. 6b). σ_{PSII} showed a subtle increase between 0°C and 7°C and remained more or less constant beyond (Fig. 6c). τ decreased linearly from ~ 4300 to $3000 \mu\text{s}$ over the investigated temperature window (Fig. 6c).

Discussion

High growth rates despite low temperatures

The three investigated species can be distinguished in two groups with regard to the width of their temperature windows and their maximal growth rates. *N. frigida* exhibited a comparably narrow thermal window (from $< 0^{\circ}\text{C}$ to 11°C , respectively; Fig. 3a; Table 1), which is in line with them occurring in the vicinity of sea-ice habitats (Assmy et al. 2017). Also, the obtained growth rates of *N. frigida* were comparably low with maximal rates of 0.54 d^{-1} (Fig. 3a).

T. hyalina and *M. pusilla* exhibited wider temperature windows in comparison *N. frigida* ($< 1\text{--}12^{\circ}\text{C}$ and 14°C , respectively; Figs. 1a, 2a; Table 1). This may reflect the strains originating from Kongsfjorden (Svalbard), which is influenced by warmer North Atlantic water masses and remains typically ice free (Payne and Roesler 2019; Tverberg et al. 2019). Both species also exhibited impressively high maximum growth rates of 1.4 d^{-1} (*T. hyalina*; Fig. 1a) and 1.02 d^{-1} (*M. pusilla*; Fig. 2a), which is in line with findings of previous studies on these isolates (Hoppe et al. 2018; Wolf et al. 2018, 2022). Such high growth rates at polar temperatures, which translate into more than 2.0 and 1.5 cell divisions per day, respectively, contradict the common notion of generally higher growth rates in warmer regions (Eppley 1972; Thomas et al. 2012). In fact, maximal growth rates observed in temperate *Thalassiosira* sp. and *Micromonas* sp. were in the same range or even lower at much higher temperatures but otherwise comparable nutrient and light conditions (Boyd et al. 2013; Baker et al. 2016; Demory et al. 2017). Consequently, the physiology of *T. hyalina* and *M. pusilla* must have evolved to compensate the thermodynamic challenges of high latitudes. One mechanism to achieve high growth rates under low temperatures could involve an upregulation of the C-fixation machinery (i.e., content of RuBisCO) as observed in a polar diatom (Young et al. 2015). Such remarkably high regulatory potential might be the foundation of the generally observed high plasticity of Arctic coastal phytoplankton assemblages (Hoppe et al. 2018) and particularly of *T. hyalina* (Wolf et al. 2018, 2022).

Table 1. Calculated optimal temperature for growth rate (T_{opt}), maximal temperature (T_{max}) as well as maximal growth rate (μ_{max}) at T_{opt} of *Thalassiosira hyalina*, *Micromonas pusilla*, and *Nitzschia frigida* according to Norberg et al. (2004). T_{window} denotes the total thermal scope, derived from $T_{\text{max}} - T_{\text{min}}$ (T_{min} was defined as -1.8°C , i.e., the freezing point of salt water at salinity 32).

Species	μ_{max} (d^{-1})	T_{opt} ($^{\circ}\text{C}$)	T_{max} ($^{\circ}\text{C}$)	T_{window} ($\Delta^{\circ}\text{C}$)
<i>T. hyalina</i>	1.22	7.0	14.5	16.3
<i>M. pusilla</i>	1.04	7.6	14.2	16.1
<i>N. frigida</i>	0.40	4.3	11.5	13.3

Interplay of cell division and biomass production rates shapes the response of biomass quotas

In contrast to the bell-shaped temperature response patterns observed in the growth rates of all species, other functional traits differed remarkably in their temperature responses. *T. hyalina* exhibited U-shaped thermal responses in their POC quotas over wide temperature ranges (Fig. 1b), which contrasts with the bell-shaped response curves of the growth rates: When growth rates were high, POC quotas were low and vice versa. This diverging pattern of the cellular POC quota is a result of the underlying physiological processes, namely cell division and biomass production. Even though, these underlying processes both followed a bell-shaped temperature response curve (Fig. 1a,b), they differ in their temperature sensitivities. More precisely, cell division is more temperature sensitive than biomass production in this species. As a consequence, cell division ceases faster than biomass production toward extreme temperatures, resulting in high POC quotas. Thus, the temperature responsiveness of cell division exerted a stronger control on elemental quotas than biomass production rates in *T. hyalina*. This phenomenon of U-shaped temperature responses of POC quotas was previously observed in the temperate phytoplankton *Phaeodactylum tricornutum*, *Pavlova lutheri*, and *Thalassiosira pseudonana* (Thompson et al. 1992; Atkinson et al. 2003; Carvalho and Malcata 2003).

M. pusilla not only exhibited bell-shaped temperature response patterns in growth and production rates similar as *T. hyalina*, but also exhibited a bell-shaped temperature response pattern in POC quotas (Fig. 2a,b). In this case, biomass production was more temperature sensitive and ceased earlier than cell division, leading to cells with lowered POC quotas at the edges of the temperature window. Thus, in this species, POC production exerted a stronger control on patterns of biomass quotas than cell division.

N. frigida also exhibited more or less bell-shaped temperature response patterns in both growth rates as well as biomass production rates. The optimum temperatures of these two processes were, however, distinct from each other, resulting in a linear increase of POC quotas with temperature (Fig. 3a,b). This finding is at odds with the common notion that high quotas reflect healthy cells. Our data, instead, show that high quotas are the result of gradually ceasing cell division while photosynthesis and subsequent biomass production are still maintained. PON quotas, however, were not increased in response to temperature in *N. frigida*, resulting in an increased POC : PON ratio of up to 15 mol mol^{-1} at 11°C (Fig. 3c). This indicates an enormous imbalance between net POC and PON production under rising temperatures with potential consequences on the nutritional value (Kwiatkowski et al. 2018; Boersma and Meunier 2020).

While the temperature response patterns of POC quotas differed remarkably between species, the principle of their emergence is generic for all species: Biomass quotas (here POC quotas) result from the interplay of the processes of cell

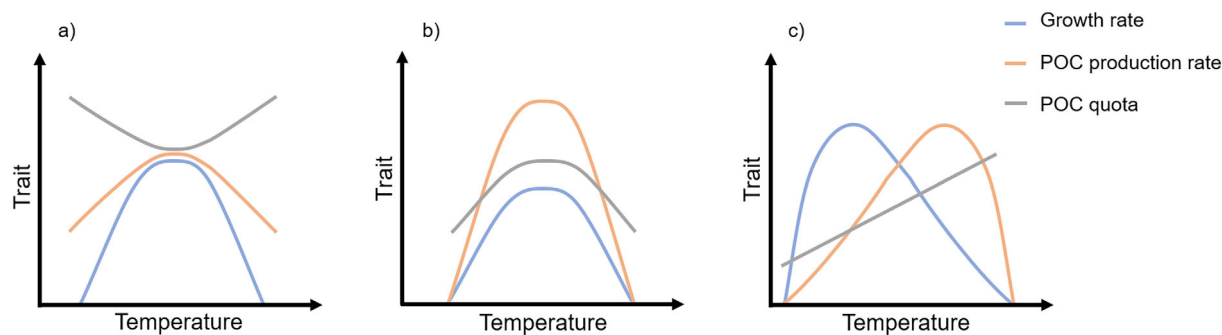


Fig. 7. Conceptualization of the interplay of growth rates (blue), POC production rates (orange) and POC quotas (gray), when POC quotas exhibit a (a) U-shaped temperature response, (b) bell-shaped temperature response or (c) linear temperature response.

division and biomass production (in this study calculated in accordance to Morel (1987)). While these two processes are largely independent and can differ in their temperature sensitivities, their combined effect and relation to each other determines the shape of the temperature response pattern of biomass quotas. Despite this comparably simple mechanistic relation, the interplay of these processes with different temperature response patterns (slope, width, and optimum temperature) manifests into diverse temperature response patterns of POC quotas. We have conceptualized these patterns in Fig. 7: If the temperature response pattern of the growth rate exhibits a steeper slope than the one of the POC production rate (i.e., cell division is more temperature sensitive than biomass production), POC quotas will exhibit a U-shaped temperature response pattern (Fig. 7a, *T. hyalina*). If the temperature response pattern of the growth rate exhibits a less steep slope than the one of POC production rate (i.e., the process of cell division is less temperature sensitive than biomass production), POC quotas will exhibit a bell-shaped temperature response pattern (Fig. 7b, *M. pusilla*). Different optimum temperatures for growth and POC production rates will result in linear trends in POC quotas (Fig. 7c, *N. frigida*). If temperature response patterns of growth rates and POC production rates were equal in shape and form, however, POC quotas would remain constant over the whole investigated temperature range (example not shown).

High temperatures cause profound shifts in photophysiology

In all species, the maximum potential quantum yield of photosystem II (F_v/F_m) was rather constant over large parts of the investigated temperature range, and only slightly decreased beyond the optimal growth temperatures (Figs. 4a, 5a, 6a). Thus, the functionality of the photosynthetic apparatus remained high over the investigated temperature range, even though cells experienced a slightly lowered efficiency under heat stress. The electron transport rate under in situ irradiance (ETR), however, followed a bell-shaped curve over large parts of the temperature window in all species

(Figs. 4b, 5b, 6b), similar to the rates of cell division and POC production. Despite species-specific differences in slope and width of the ETR temperature response, its optimal temperature seemed to be generally 1–3°C higher than the respective optimal temperatures of cell division and POC production. This proves the existence of diverging optimal temperatures in different photosynthetic subprocesses within one cell. The differences in temperature sensitivities between ETR and POC production, in turn, advocate arising imbalances between photosynthetic light-dependent and light-independent reactions toward the edges of the temperature window. More specifically, the discrepancies between “both sides of photosynthesis” cause an overreduction of the photosynthetic electron transport chain at temperature extremes, likely giving rise to oxidative stress. Future research should target compensatory mechanisms to deal with extreme temperatures.

In both pelagic species, the Chl *a* : POC ratio showed an increasing trend beyond optimal growth temperatures (Figs. 1c, 2c), indicating a relatively higher pigmentation per biomass. This can be caused by stronger changes in POC quotas than in Chl *a* quotas with temperature, but also shifts in light harvesting complexes or photosystem abundances are indicated. In *M. pusilla*, for instance, the absorption cross section of PSII (Fig. 5c) increased with temperature throughout the temperature range where μ is $\geq 80\%$ of μ_{max} (i.e., the green band), indicating increased antenna sizes of the light harvesting complexes. In *T. hyalina*, we did not observe such an increase in PSII absorption cross section beyond optimal temperatures (Fig. 4c), but here the increased pigmentation per biomass might be explained by increased abundances of photosystems. Such a strategy, especially the upregulation of PSI, might additionally serve to dissipate the aforementioned overreduction at highest temperatures.

In contrast to the findings for the pelagic species, the ice alga *N. frigida* responded with a strong decrease of Chl *a* : POC ratios with increasing temperatures (Fig. 3c), which can be attributed to the massively increased POC quotas at high temperatures (Fig. 3b). This increase may be a result of the cells'

attempt to deal with temperature induced redox stress: Only *N. frigida* experienced an increase of nonphotochemical quenching (NPQ) at in situ light intensity under the highest temperature (Supporting Information Fig. S2), indicating overreduction. It was previously observed that other microalgae reroute excess plastidary reductant into the mitochondria. This causes a shift in the redox state and throttles their citric acid cycle activity, which decreases the respiratory carbon loss (Bailleul et al. 2015; Curien et al. 2016), while maintaining the respiratory electron transport chain. This was especially pronounced under increased temperatures (Rehder et al. 2023) and might explain the here observed massive POC retention in *N. frigida* under high temperatures.

All three species showed a linear decrease in τ , reflecting a generally faster reopening of photosystem II with warming (Figs. 4c, 5c, 6c). This is in line with the response of temperate diatoms (Baker et al. 2016) as well as Arctic phytoplankton communities (Wolf et al. 2024) and possibly constitutes a generic feature of photosynthesis. Whether this is an acclimation response or merely a thermodynamic effect should be subject of future studies.

The here investigated species also showed a consistent increase in their fluorescence-based light acclimation indices (E_k) in response to warming until a certain threshold (Figs. 4b, 5b, 6b). E_k is the light intensity, at which photosynthesis transitions from light limitation (in situ light intensity $< E_k$) to saturation (in situ light intensity $> E_k$) (Behrenfeld et al. 2004). While it is known that E_k is affected by acclimation to different light levels (MacIntyre et al. 2002; Behrenfeld et al. 2008), our data show that the transition point from light limitation into light saturation is shifted to higher irradiances also with warming. In other words, high temperatures make cells more “light-limited” (as indicated by increasing E_k), thereby enabling them to exploit light intensities that would be saturating or even stressful under low temperatures (Behrenfeld et al. 2004). Despite this phenomenon being common among the investigated species, there were species-specific differences: *T. hyalina* and *N. frigida* kept E_k more or less constant up to their optimal growth temperatures, but experienced a strong increase beyond (Figs. 4b, 6b). Thereby, cells remained close to light saturation up to their temperature optimum, and only beyond, they transitioned abruptly into a thermally induced light limitation. *M. pusilla* experienced a gentle but steady increase of E_k over large parts of their thermal window (Fig. 5b). Thus, they gradually become more light-limited with warming so that the transition from light saturation at low temperature into light limitation at high temperature is smoother than in the other investigated species. Overall, phytoplankton likely benefit from a simultaneous increase of temperature and light, as these changes are projected for the large parts of the Arctic Ocean with ongoing climate change (Constable et al. 2022).

Conclusion and ecological implications

Different phytoplankton functional traits were found to differ substantially in their temperature response patterns. Particularly, physiological processes such as cell division, electron transport rates or biomass production rates generally followed optimal- or bell-shaped patterns, which differed in their optimal temperatures and/or slopes of increase or decrease. Resulting quotas such as Chl *a* and POC quotas, however, exhibited partially opposing response patterns between species, depending on the relation of their underlying physiological processes. This emphasizes the necessity for holistic assessments including multiple temperatures, species, and functional traits, all of which should then also be considered for biogeochemical modeling approaches or the evaluation of remote sensing data.

Generally, some of the investigated species not only exhibited impressively high growth rates, they also covered unexpectedly wide thermal windows with rather high optimal temperatures. Part of this may be attributable to the fact that isolates originated from the Fram Strait or Svalbard fjords and are thus influenced by varying contributions of warmer North Atlantic water. Consequently, these species may generally exhibit a higher phenotypic plasticity toward temperature than phytoplankton originating from the high Arctic. Nonetheless, all investigated species seem to live below their optimal growth temperatures in the present-day Arctic Ocean. Consequently, they will likely benefit from future ocean warming up to a certain species-specific (and potentially strain-specific) threshold. Our data on photophysiology moreover indicate a synergistic effect of irradiance and temperature, which both are predicted to increase in the Arctic due to enhanced sea-ice melt as well as thermally induced stratification. This would add further support to projections of nutrients becoming a dominant limiting factor for primary production in high-latitude marine ecosystems (Tremblay et al. 2015). In the future Arctic Ocean, phytoplankton spring blooms might be characterized by higher growth rates and biomass production, but thereby nutrients are depleted faster, resulting in more intense but shorter bloom events.

Data availability statement

The data supporting the findings of this study are openly available in the Pangea Database, <https://doi.pangaea.de/10.1594/PANGAEA.968670>.

References

- Ahme, A., A. Von Jackowski, R. A. McPherson, K. K. Wolf, M. Hoppmann, S. Neuhaus, and U. John. 2023. Winners and losers of Atlantification: The degree of ocean warming affects the structure of Arctic microbial communities. *Genes* **14**: 623.

- Ahme, A., and others. 2024. Warming increases the compositional and functional variability of a temperate protist community. *Sci. Total Environ.* **926**: 171971.
- Ardyna, M., and K. R. Arrigo. 2020. Phytoplankton dynamics in a changing Arctic Ocean. *Nat. Clim. Change* **10**: 892–903. doi:10.1038/s41558-020-0905-y
- Assmy, P., and others. 2017. Leads in Arctic pack ice enable early phytoplankton blooms below snow-covered sea ice. *Sci. Rep.* **7**: 40850. doi:10.1038/srep40850
- Assmy, P., and others. 2023. Seasonal plankton dynamics in Kongsfjorden during two years of contrasting environmental conditions. *Prog. Oceanogr.* **213**: 102996.
- Atkinson, D., B. J. Ciotti, and D. J. Montagnes. 2003. Protists decrease in size linearly with temperature: ca. 2.5% C⁻¹. *Proc. R. Soc. Lond. Ser. B Biol. Sci.* **270**: 2605–2611.
- Bailleul, B., and others. 2015. Energetic coupling between plastids and mitochondria drives CO₂ assimilation in diatoms. *Nature* **524**: 366–369.
- Baker, K. G., C. M. Robinson, D. T. Radford, A. S. McInnes, C. Evenhuis, and M. A. Doblin. 2016. Thermal performance curves of functional traits aid understanding of thermally induced changes in diatom-mediated biogeochemical fluxes. *Front. Mar. Sci.* **3**: 44.
- Barton, S., and G. Yvon-Durocher. 2019. Quantifying the temperature dependence of growth rate in marine phytoplankton within and across species. *Limnol. Oceanogr.* **64**: 2081–2091.
- Barton, S., J. Jenkins, A. Buckling, C.-E. Schaum, N. Smirnov, J. A. Raven, and G. Yvon-Durocher. 2020. Evolutionary temperature compensation of carbon fixation in marine phytoplankton. *Ecol. Lett.* **23**: 722–733. doi:10.1111/ele.13469
- Barton, S., D. Padfield, A. Masterson, A. Buckling, N. Smirnov, and G. Yvon-Durocher. 2023. Comparative experimental evolution reveals species-specific idiosyncrasies in marine phytoplankton adaptation to warming. *Glob. Chang. Biol.* **29**: 5261–5275.
- Behrenfeld, M. J., O. Prasil, M. Babin, and F. Bruyant. 2004. In search of a physiological basis for covariations in light-limited and light-saturated photosynthesis 1. *J. Phycol.* **40**: 4–25.
- Behrenfeld, M. J., K. H. Halsey, and A. J. Milligan. 2008. Evolved physiological responses of phytoplankton to their integrated growth environment. *Philos. Trans. R. Soc. B Biol. Sci.* **363**: 2687–2703.
- Boersma, M., and C. L. Meunier. 2020. Zooplankton–phytoplankton interactions in a changing world, p. 28–52. *In* *Zooplankton ecology*. CRC Press.
- Boyd, P. W., and others. 2013. Marine phytoplankton temperature versus growth responses from polar to tropical waters—Outcome of a scientific community-wide study. *PLoS One* **8**: e63091.
- Carvalho, A. P., and F. X. Malcata. 2003. Kinetic modeling of the autotrophic growth of *Pavlova lutheri*: Study of the combined influence of light and temperature. *Biotechnol. Prog.* **19**: 1128–1135.
- Constable, A. J., and others. 2022. Cross-chapter paper 6: Polar regions. *In* IPCC AR WGII. Cambridge Univ. Press.
- Cooley, S., and others. 2022. Oceans and coastal ecosystems and their services. *In* IPCC AR6 WGII. Cambridge Univ. Press.
- Curien, G., and others. 2016. The water to water cycles in microalgae. *Plant Cell Physiol.* **57**: 1354–1363.
- Demory, D., and others. 2017. Temperature is a key factor in *Micromonas*–virus interactions. *ISME J.* **11**: 601–612. doi:10.1038/ismej.2016.160
- Eppley, R. W. 1972. Temperature and phytoplankton growth in the sea. *Fish. Bull.* **70**: 1063–1085.
- Falkowski, P. G., R. T. Barber, and V. Smetacek. 1998. Biogeochemical controls and feedbacks on ocean primary production. *Science* **281**: 200–206. doi:10.1126/science.281.5374.200
- Genty, B., J.-M. Briantais, and N. R. Baker. 1989. The relationship between the quantum yield of photosynthetic electron transport and quenching of chlorophyll fluorescence. *Biochim. Biophys. Acta Gen. Subj.* **990**: 87–92. doi:10.1016/S0304-4165(89)80016-9
- Guillard, R. R., and J. H. Ryther. 1962. Studies of marine planktonic diatoms: I. *Cyclotella nana* Hustedt, and *Detonula confervacea* (Cleve) Gran. *Can. J. Microbiol.* **8**: 229–239.
- Hancke, K., and R. N. Glud. 2004. Temperature effects on respiration and photosynthesis in three diatom-dominated benthic communities. *Aquat. Microb. Ecol.* **37**: 265–281.
- Hare, C. E., K. Leblanc, G. R. DiTullio, R. M. Kudela, Y. Zhang, P. A. Lee, S. Riseman, and D. A. Hutchins. 2007. Consequences of increased temperature and CO₂ for phytoplankton community structure in the Bering Sea. *Mar. Ecol. Prog. Ser.* **352**: 9–16.
- Hegseth, E. N., and A. Sundfjord. 2008. Intrusion and blooming of Atlantic phytoplankton species in the high Arctic. *J. Mar. Syst.* **74**: 108–119. doi:10.1016/j.jmarsys.2007.11.011
- Hobday, A. J., and others. 2016. A hierarchical approach to defining marine heatwaves. *Prog. Oceanogr.* **141**: 227–238.
- Holding, J. M., C. M. Duarte, J. M. Arrieta, R. Vaquer-Sunyer, A. Coello-Camba, P. Wassmann, and S. Agustí. 2013. Experimentally determined temperature thresholds for Arctic plankton community metabolism. *Biogeosciences* **10**: 357–370. doi:10.5194/bg-10-357-2013
- Hoppe, C. J. M., C. M. Flintrop, and B. Rost. 2018. The Arctic picoeukaryote *Micromonas pusilla* benefits synergistically from warming and ocean acidification. *Biogeosciences* **15**: 4353–4365.
- Hoppe, H.-G., K. Gocke, R. Koppe, and C. Begler. 2002. Bacterial growth and primary production along a north–south transect of the Atlantic Ocean. *Nature* **416**: 168–171. doi:10.1038/416168a

- Kling, J. D., M. D. Lee, F. Fu, M. D. Phan, X. Wang, P. Qu, and D. A. Hutchins. 2020. Transient exposure to novel high temperatures reshapes coastal phytoplankton communities. *ISME J.* **14**: 413–424. doi:10.1038/s41396-019-0525-6
- Knap, A., A. Michaels, A. Close, H. Ducklow, and A. Dickson. 1996. Protocols for the joint global ocean flux study (JGOFS) core measurements. JGOFS. Reprint of the IOC manuals and guides no. 29, UNESCO 1994, 19.
- Kolber, Z. S., O. Prášil, and P. G. Falkowski. 1998. Measurements of variable chlorophyll fluorescence using fast repetition rate techniques: Defining methodology and experimental protocols. *Biochim. Biophys. Acta Bioenergetics* **1367**: 88–106.
- Kwiatkowski, L., O. Aumont, L. Bopp, and P. Ciais. 2018. The impact of variable phytoplankton stoichiometry on projections of primary production, food quality, and carbon uptake in the global ocean. *Global Biogeochem. Cycl.* **32**: 516–528.
- Lewis, K., G. Van Dijken, and K. R. Arrigo. 2020. Changes in phytoplankton concentration now drive increased Arctic Ocean primary production. *Science* **369**: 198–202.
- Listmann, L., M. LeRoch, L. Schlüter, M. K. Thomas, and T. B. H. Reusch. 2016. Swift thermal reaction norm evolution in a key marine phytoplankton species. *Evol. Appl.* **9**: 1156–1164. doi:10.1111/eva.12362
- MacIntyre, H. L., T. M. Kana, T. Anning, and R. J. Geider. 2002. Photoacclimation of photosynthesis irradiance response curves and photosynthetic pigments in microalgae and cyanobacteria 1. *J. Phycol.* **38**: 17–38.
- Maxwell, K., and G. N. Johnson. 2000. Chlorophyll fluorescence—A practical guide. *J. Exp. Bot.* **51**: 659–668. doi:10.1093/jexbot/51.345.659
- McKew, B. A., and others. 2013. The trade-off between the light-harvesting and photoprotective functions of fucoxanthin-chlorophyll proteins dominates light acclimation in *Emiliania huxleyi* (clone CCMP 1516). *New Phytol.* **200**: 74–85. doi:10.1111/nph.12373
- Morel, F. M. 1987. Kinetics of nutrient uptake and growth in phytoplankton 1. *J. Phycol.* **23**: 137–150.
- Moreno, H. D., S. Rokitta, N. Tremblay, M. Boersma, E. Groß, H. C. Klip, K. H. Wiltshire, and C. L. Meunier. 2024. Higher temperature, increased CO₂, and changing nutrient ratios alter the carbon metabolism and induce oxidative stress in a cosmopolitan diatom. *Limnol. Oceanogr.* **69**: 121–139. doi:10.1002/lno.12463
- Norberg, E., G. Rogers, R. Goodling, J. Cooper, and P. Madsen. 2004. Genetic parameters for test-day electrical conductivity of milk for first-lactation cows from random regression models. *J. Dairy Sci.* **87**: 1917–1924.
- Nöthig, E.-M., and others. 2015. Summertime plankton ecology in Fram Strait—A compilation of long- and short-term observations. *Polar Res.* **34**: 23349. doi:10.3402/polar.v34.23349
- Orkney, A., T. Platt, B. E. Narayanaswamy, I. Kostakis, and H. A. Bouman. 2020. Bio-optical evidence for increasing *Phaeocystis* dominance in the Barents Sea. *Philos. Trans. R. Soc. A Math. Phys. Eng. Sci.* **378**: 20190357. doi:10.1098/rsta.2019.0357
- Oxborough, K. 2012. FastPro8 GUI and FRRf3 systems documentation. Chelsea Technologies Group Ltd.
- Padfield, D., G. Yvon-Durocher, A. Buckling, S. Jennings, and G. Yvon-Durocher. 2016. Rapid evolution of metabolic traits explains thermal adaptation in phytoplankton. *Ecol. Lett.* **19**: 133–142. doi:10.1111/ele.12545
- Payne, C. M., and C. S. Roesler. 2019. Characterizing the influence of Atlantic water intrusion on water mass formation and phytoplankton distribution in Kongsfjorden, Svalbard. *Cont. Shelf Res.* **191**: 104005. doi:10.1016/j.csr.2019.104005
- Rantanen, M., A. Y. Karpechko, A. Lipponen, K. Nordling, O. Hyvärinen, K. Ruosteenoja, T. Vihma, and A. Laaksonen. 2022. The Arctic has warmed nearly four times faster than the globe since 1979. *Commun. Earth Environ.* **3**: 168. doi:10.1038/s43247-022-00498-3
- Raven, J. A., and R. J. Geider. 1988. Temperature and algal growth. *New Phytol.* **110**: 441–461.
- Rehder, L., B. Rost, and S. D. Rokitta. 2023. Abrupt and acclimation responses to changing temperature elicit divergent physiological effects in the diatom *Phaeodactylum tricorutum*. *New Phytol.* **239**: 1005–1013.
- Rokitta, S. D., and B. Rost. 2012. Effects of CO₂ and their modulation by light in the life-cycle stages of the coccolithophore *Emiliania huxleyi*. *Limnol. Oceanogr.* **57**: 607–618.
- Rokitta, S. D., C. H. Grossmann, E. Werner, J. Moye, G. Castellani, E. M. Nöthig, and B. Rost. 2023. Future warming stimulates growth and photosynthesis in an Arctic microalga more strongly than changes in light intensity or pCO₂. *Limnol. Oceanogr.* **68**: 2789–2799.
- Schaum, C. E., and others. 2017. Adaptation of phytoplankton to a decade of experimental warming linked to increased photosynthesis. *Nat. Ecol. Evol.* **1**: 0094. doi:10.1038/s41559-017-0094
- Schuback, N., C. J. Hoppe, J. É. Tremblay, M. T. Maldonado, and P. D. Tortell. 2017. Primary productivity and the coupling of photosynthetic electron transport and carbon fixation in the Arctic Ocean. *Limnol. Oceanogr.* **62**: 898–921.
- Soltwedel, T., and others. 2016. Natural variability or anthropogenically-induced variation? Insights from 15 years of multidisciplinary observations at the arctic marine LTER site HAUSGARTEN. *Ecol. Indic.* **65**: 89–102. doi:10.1016/j.ecolind.2015.10.001
- Stock, C. A., J. P. Dunne, and J. G. John. 2014. Drivers of trophic amplification of ocean productivity trends in a changing climate. *Biogeosciences* **11**: 7125–7135. doi:10.5194/bg-11-7125-2014
- Suggett, D. J., H. L. MacIntyre, and R. J. Geider. 2004. Evaluation of biophysical and optical determinations of light

- absorption by photosystem II in phytoplankton. *Limnol. Oceanogr. Methods* **2**: 316–332.
- Syvertsen, E. E. 1991. Ice algae in the Barents Sea: Types of assemblages, origin, fate and role in the ice-edge phytoplankton bloom. *Polar Res.* **10**: 277–288. doi:10.1111/j.1751-8369.1991.tb00653.x
- Tedesco, L., M. Vichi, and E. Scoccimarro. 2019. Sea-ice algal phenology in a warmer arctic. *Sci. Adv.* **5**: eaav4830. doi:10.1126/sciadv.aav4830
- Thomas, M. K., C. T. Kremer, C. A. Klausmeier, and E. Litchman. 2012. A global pattern of thermal adaptation in marine phytoplankton. *Science* **338**: 1085–1088. doi:10.1126/science.1224836
- Thompson, P. A., M. x. Guo, P. J. Harrison, and J. N. Whyte. 1992. Effects of variation in temperature. II. On the fatty acid composition of eight species of marine phytoplankton 1. *J. Phycol.* **28**: 488–497.
- Tremblay, J.-É., L. G. Anderson, P. Matrai, P. Coupel, S. Bélanger, C. Michel, and M. Reigstad. 2015. Global and regional drivers of nutrient supply, primary production and CO₂ drawdown in the changing Arctic Ocean. *Prog. Oceanogr.* **139**: 171–196.
- Trimborn, S., S. Thoms, T. Brenneis, J. P. Heiden, S. Beszteri, and K. Bischof. 2017. Two Southern Ocean diatoms are more sensitive to ocean acidification and changes in irradiance than the prymnesiophyte *Phaeocystis antarctica*. *Phycol. Plant.* **160**: 155–170. doi:10.1111/ppl.12539
- Tverberg, V., R. Skogseth, F. Cottier, A. Sundfjord, W. Walczowski, M. E. Inall, E. Falck, O. Pavlova, and F. Nilsen. 2019. The Kongsfjorden transect: Seasonal and inter-annual variability in hydrography, p. 49–104. *In* The cosystem of Kongsfjorden. Springer.
- Vader, A., M. Marquardt, A. R. Meshram, and T. M. Gabrielsen. 2015. Key Arctic phototrophs are widespread in the polar night. *Polar Biol.* **38**: 13–21. doi:10.1007/s00300-014-1570-2
- Van Leeuwe, M. A., and others. 2018. Microalgal community structure and primary production in Arctic and Antarctic sea ice: A synthesis. *Elem. Sci. Anthropol.* **6**: 4.
- Wassmann, P., and M. Reigstad. 2011. Future Arctic Ocean seasonal ice zones and implications for pelagic-benthic coupling. *Oceanography* **24**: 220–231.
- Wiedmann, I., E. Ershova, B. A. Bluhm, E.-M. Nöthig, R. R. Gradinger, K. Kosobokova, and A. Boetius. 2020. What feeds the benthos in the Arctic Basins? Assembling a carbon budget for the deep Arctic Ocean. *Front. Mar. Sci.* **7**: 224.
- Wolf, K. K., C. J. Hoppe, and B. Rost. 2018. Resilience by diversity: Large intraspecific differences in climate change responses of an Arctic diatom. *Limnol. Oceanogr.* **63**: 397–411.
- Wolf, K. K., S. D. Rokitta, C. J. Hoppe, and B. Rost. 2022. Pelagic and ice-associated microalgae under elevated light and pCO₂: Contrasting physiological strategies in two Arctic diatoms. *Limnol. Oceanogr.* **67**: 1895–1910.
- Wolf, K. K. E., C. J. M. Hoppe, L. Rehder, C.-E. Schaum, U. John, and B. Rost. 2024. Heatwave responses of Arctic phytoplankton communities are driven by combined impacts of warming and cooling. *Sci. Adv.* **10**: ead15904. doi:10.1126/sciadv.adl5904
- Young, J. N., J. A. Goldman, S. A. Kranz, P. D. Tortell, and F. M. Morel. 2015. Slow carboxylation of Rubisco constrains the rate of carbon fixation during Antarctic phytoplankton blooms. *New Phytol.* **205**: 172–181.

Acknowledgments

We thank Tina Brenneis, Lorenz Eckardt, and Laura Wischnewski for their technical support in measurements of Chl *a* as well as POC and PON. Furthermore, we thank Luka Šupraha and the Norwegian Culture Collection of Algae for providing the *Nitzschia frigida* strain. The funding was provided by Alfred Wegener Institute, Helmholtz Centre for Polar and Marine Research. Open Access funding enabled and organized by Projekt DEAL.

Conflict of Interest

None declared.

Submitted 12 January 2024

Revised 12 April 2024

Accepted 29 June 2024

Associate editor: Bingzhang Chen